Supplementary Information

S1. Notes on Evaluation With Python

All evaluation that involved Python was performed using version 3.11.3 within a self-developed project that relied on the following dependencies required for this investigation: ipykernel (version 7.0.1.); ipympl (version 0.9.8); ipython (version 9.6.0); joblib (version 1.5.2); lmfit (version 1.3.4); matplotlib (version 3.10.7); notebook (7.4.7); numpy (version 2.3.4); openpyxl (version 3.1.5); pandas (version 2.3.3); pybaselines (version 1.2.1); scikit-learn (version 1.8.0); scipy (version 1.16.2); spe2py (version 2.0.0). There is currently no intention to release the project into public domain, but code can partially be made available upon request to the first author.

S2. Spectra Comparison of Different Polymers

In order to establish whether the structured background observed for the calibration standards is unique for polyimide as the matrix, similarly prepared polymer films were analyzed with the same ablation and detection parameters. Contrary to the film standard preparation laid out in the main manuscript (see section 2.1), polymer solutions were prepared with a polymer concentration of 100 $mg \cdot g^{-1}$ in N-Methyl-2-pyrrolidone (NMP), which were directly applied to Si wafer pieces. Additionally, the films were not spin-coated, but rather drop-casted, i.e., 40 µL of polymer solution were pipetted onto the wafer pieces and the solvent was then evaporated on a hot plate set to 100 °C for 15 min.

The polymers used for this experiment were as follows: polyethersulfone, PES (Goodfellow Cambridge Limited, Huntingdon, United Kingdom); polyimide, PI (P84 200 mesh, Ensinger Sintimid, Lenzing, Austria); polymethylmethacrylate, PMMA (Acros Organics, Fair Lawn (NJ), USA); polyphenylene sulfone, PPSU (Goodfellow Cambridge Limited, Huntingdon, United Kingdom); polystyrene, PS (Thermo Fisher Scientific, Ward Hill (MA), USA); polysulfone, PSU (Acros Organics, Fair Lawn (NJ), USA); polyurethane, PU (Goodfellow Cambridge Limited, Huntingdon, United Kingdom); polyvinyl chloride, PVC (Acros Organics, Fair Lawn (NJ), USA); polyvinylidene chloride, PVDC (Goodfellow Cambridge Limited, Huntingdon, United Kingdom); polyvinylpyrrolidone, PVP (Sigma-Aldrich, St. Louis (MO), USA). Furthermore, to test the impact of the solvent (and rule out F contamination by the solvent), a PS solution was prepared with toluene and processed in the same way.

Judging from the comparison shown in Figure S1, the background in the entire wavelength range is similar for all the investigated polymers, especially in the region specific for the most intense F I emission. However, there are some noticeable differences: (1) the absolute intensity is markedly lower for PMMA and PVP for the full spectrum; (2) the “F I emission” is higher for PMMA, PU, PVC, PVDC, and PVP, though still comparable to PI and therefore a blank standard used for calibration; (3) the background seems less feature-rich for PVC and to a lesser extent also PVDC (especially compared to PVP). All in all, this comparison supports the hypothesis that the structured background found in the vicinity of the F I emission lines is not polyimide-specific, but rather an occurrence for polymers in general. Since the spectra of PS prepared in NMP and toluene are highly comparable, an impact of (or contamination by) the solvent can be disregarded.

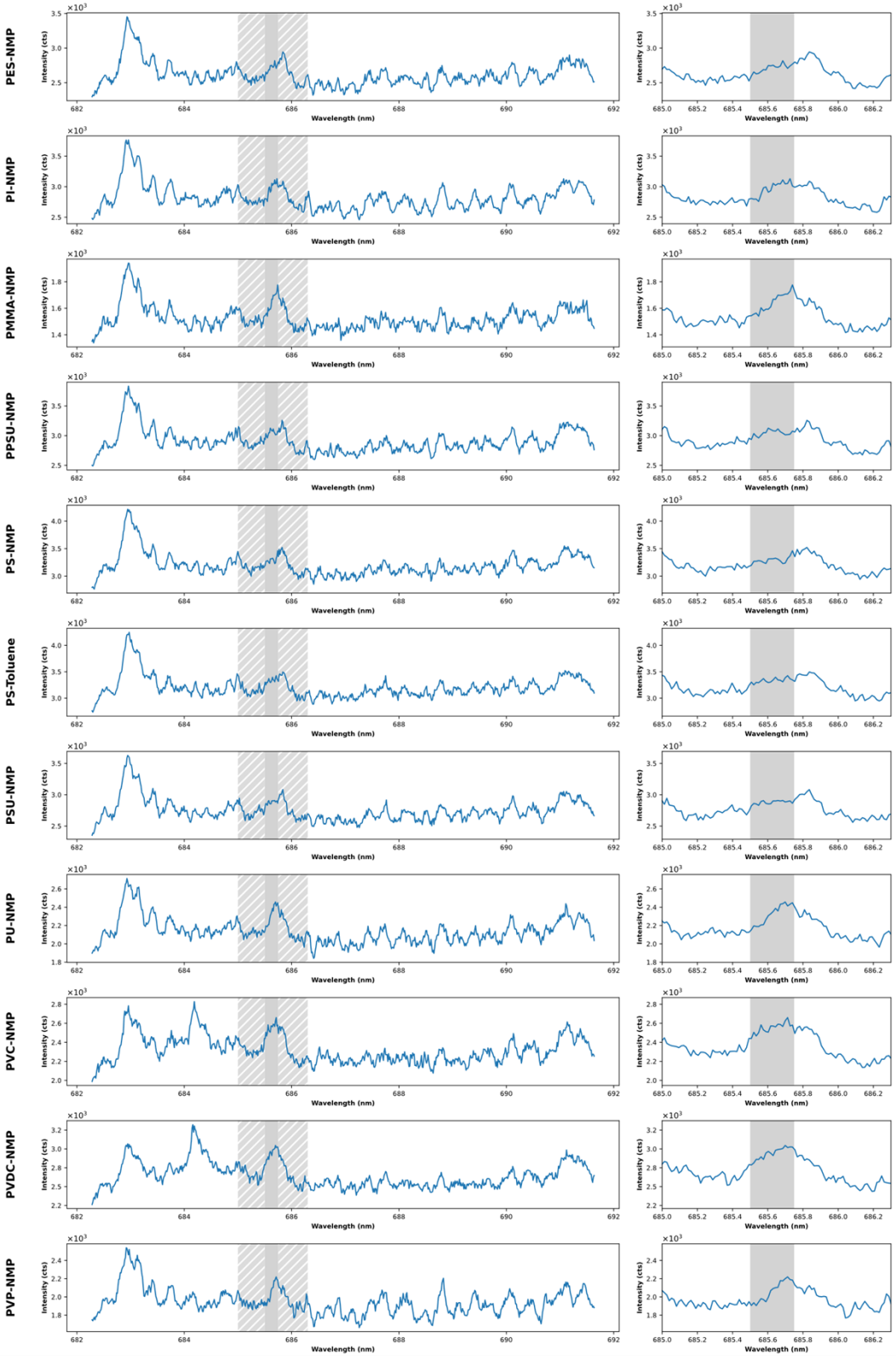

Figure S1: Comparison of spectra obtained from ablating different polymers. The polymer and corresponding solvent employed for dissolution are given to the left of each row. The striped shaded area in plot of the left column marks the range shown in the zoomed-in plots of the right column. The fully shaded area highlights the wavelength range specific to the most intense F I emission in the measured spectra. Spectra were acquired with a laser energy of 8.21 mJ, ablation atmosphere pressure of 50 mbar, gate delay of 0.4 µs, and gate width of 2.0 µs and represent the average spectrum of 42 laser shots.

S3. Profilometric Measurements Regarding the Influence of Ablation Atmosphere on Ablation Rate

To investigate whether the ablation atmosphere has an impact on the ablation rate for the prepared polyimide-based standards, profilometric measurements with a Dektak XT (Bruker, Billerica (MA), USA) were performed. Three film standards were ablated with pulse energies of 0.83, 2.34, 5.37, and 8.21 mJ and ablation atmosphere pressures of 50, 250, and 1000 mbar. Each polymer film experienced three successive laser scan lines with each energy, but was subjected to different pressures. The polymer films were subsequently mapped with the profilometer by performing 12 scans (with a spacing of 78 µm) perpendicular to the direction of laser scanning with a resolution of 0.3 µm.

These maps were then processed via Gwyddion (version 2.67), by directly loading the OPDX files output by the profilometer. To eliminate the profilometer's stage tilt, first a coarse facet levelling was performed. Afterwards, the ablation craters were masked by marking grains via a (height) threshold. After manual mask adjustment (to remove outliers), a second levelling step was performed by fitting a polynomial background (with seven degrees in horizontal and vertical direction). Finally, the levelled maps were exported to XYZ files and read into the Python project outlined in section 1. The 12 scans were then averaged for all three atmosphere pressures separately. Figure S2 illustrates the average profilometric traces for the different ablation atmospheres and laser energies and demonstrates that no there is no significant variation of the ablation rate with pressure for the ablation of the polyimide standards.

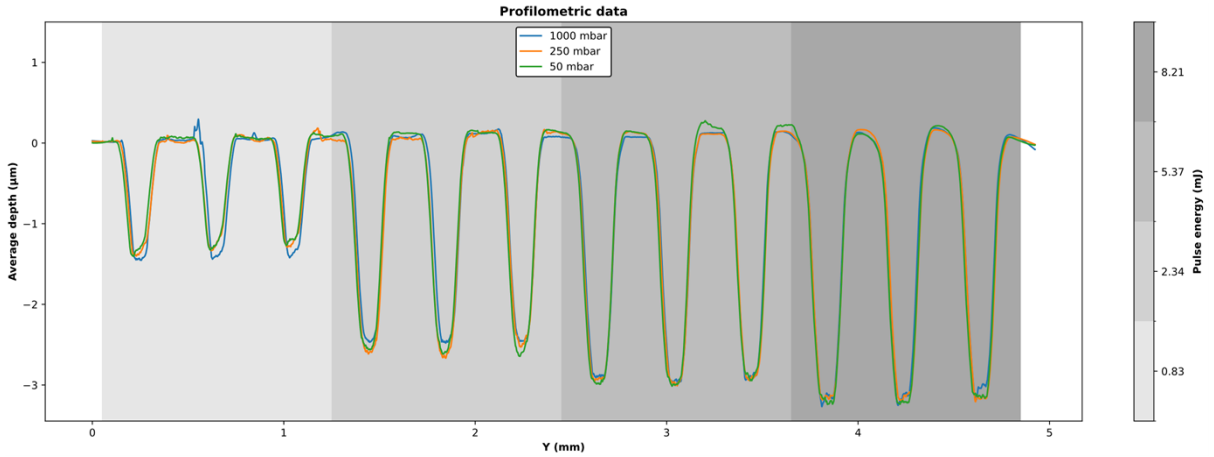

Figure S2: Average profilometric traces (n = 12) for different ablation atmospheres and laser energies. The different shades of grey highlight the craters corresponding to the same laser energy, as denoted in the color bar to the right.

S4. Parameter Optimization: Laser Energy and Ablation Atmosphere Pressure

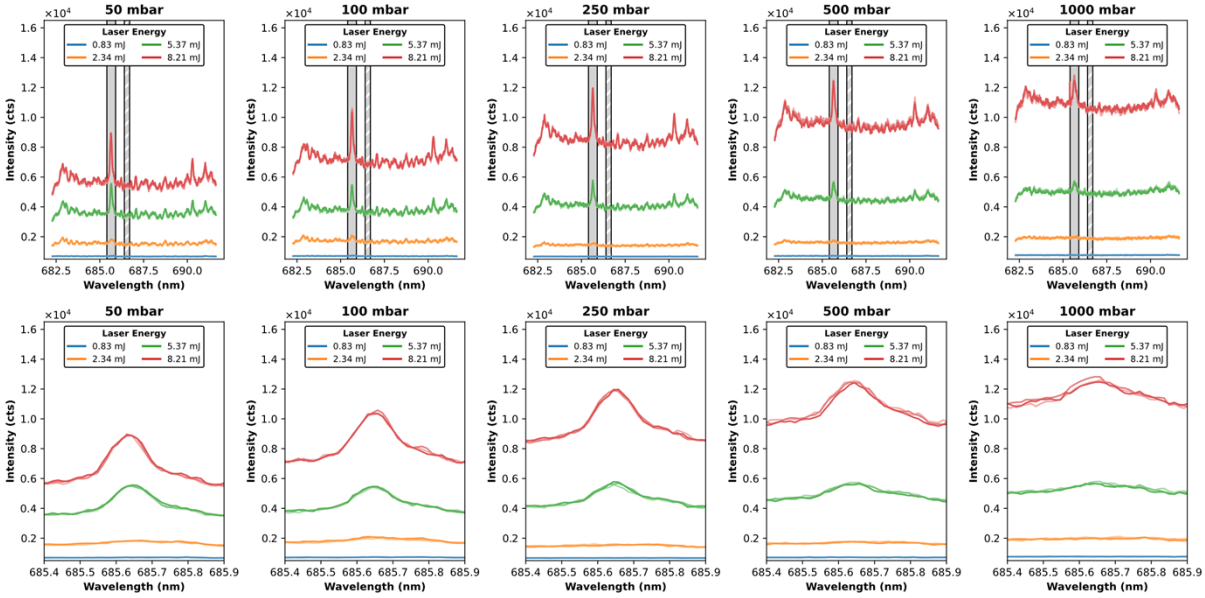

Figure S3: Comparison of spectra for different laser energies and ablations atmosphere pressures. The top row show the full spectra, whereas the bottom row represents the zoomed-in region fully shaded in the top row. The striped region in the top row highlights the area used for the calculation of the signal-to-background ratio and noise (686.4-686.7 nm). Spectra represent the average of 42 shots from the analysis of a standard containing 2,145 ppm F, acquired with a gate delay of 0.3 µs and a gate width of 5.0 µs. The five repeat measurements of each laser energy use the same base color, but different opacity.

S5. Parameter Optimization: Gate Delay and Ablation Atmosphere Pressure

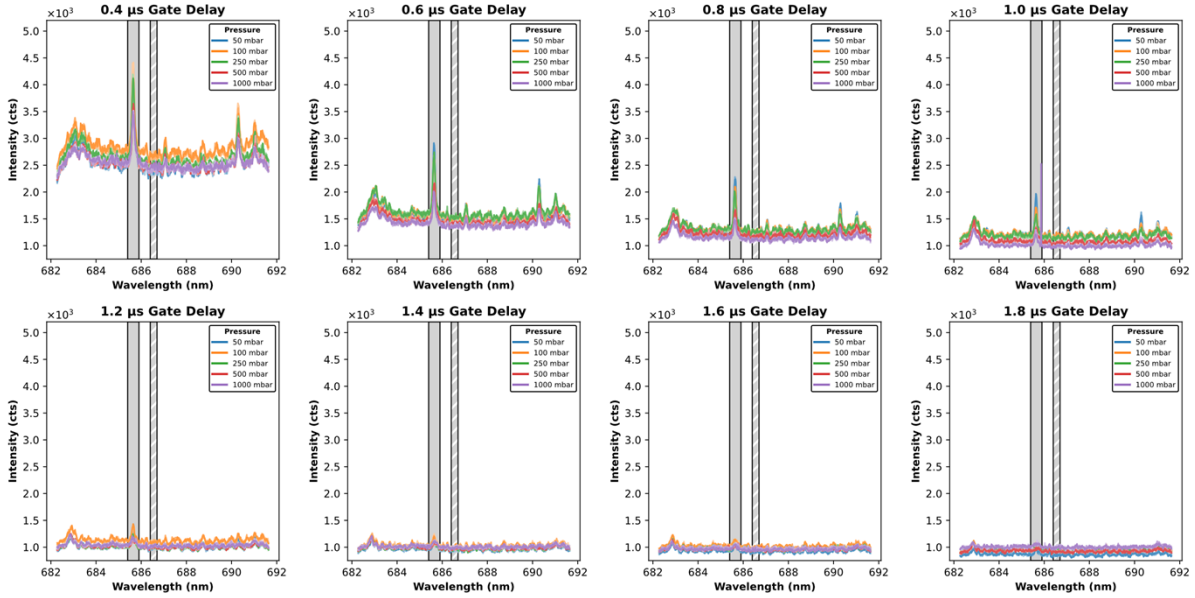

Figure S4: Comparison of spectra for different ablation atmosphere pressures and gate delays. The respective gate delays are given in the subplot titles. The grey shaded area represents the "signal" region, whereas the striped region highlights the area used for the calculation of the signal-to-background ratio and noise. Spectra represent the average of 42 shots from the analysis of a standard containing 2,145 ppm F, acquired with a laser energy of 8.21 mJ and a gate width of 0.5 µs. The five repeat measurements of each laser energy use the same base color, but different opacity.

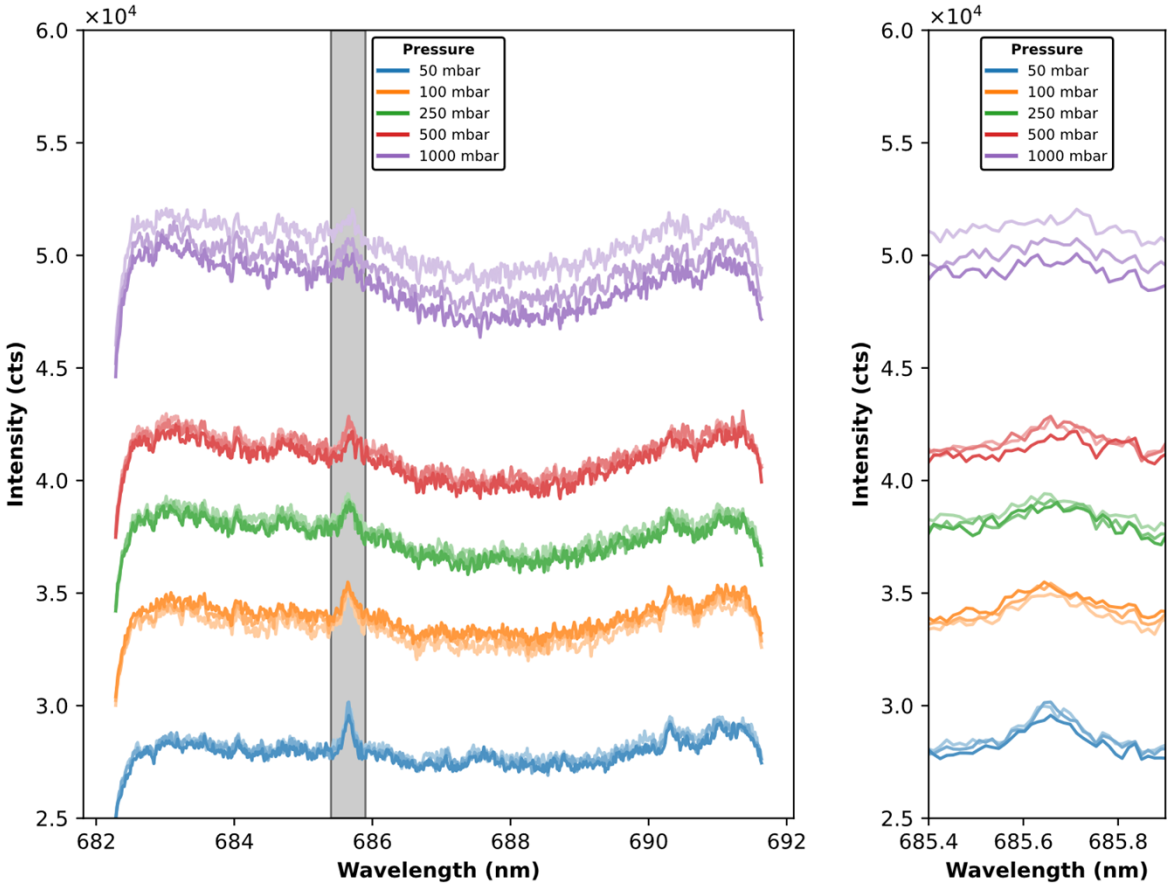

Figure S5: Comparison of spectra at different atmosphere pressures, measured with a gate delay of 0.2 µs. Spectra represent the average of 42 shots from the analysis of a standard containing 2,145 ppm F, acquired with a laser energy of 8.21 mJ and a gate width of 0.5 µs. The five repeat measurements of each laser energy use the same base color, but different opacity. The area shaded grey indicates the wavelength range covered by the zoomed-in subplot to the right.

S6. Discussion of Normalization and Background Subtraction Approaches

The review by Guézénoc, Gallet-Budynek, and Bousquet provides an excellent framework to compare different normalization approaches. They include a selection of 20 articles that dealt with normalization in LIBS and while that list is by no means complete, a total of seven strategies were collated, which include the normalization to: (1) the maximum; (2) the minimum; (3) the background; (4) the total area (i.e., the sum of all intensities recorded by the spectrometer); (5) the Euclidian norm; (6) an internal standard; and (7) the standard normal variate (SNV). The latter transforms the spectrum in such a way that the mean is zero and the standard deviation is one. Broadly speaking, these are the most common approaches found in LIBS literature. [1]

For this investigation, using an internal standard is not feasible since the standard cannot be added to the film samples themselves. Besides, as Hahn and Omenetto point out in their fundamental review of LIBS [2], the choice of a suitable internal standard is incredibly limited in most settings and the criteria for selection are almost never fulfilled. One could argue that the C I emission (as seen in, e.g., Figure S1) could be taken advantage of, but as the emission is not baseline resolved (and overlaps with the structured background), this is not an ideal choice either.

When dealing with normalization strategies that take into account the entire spectrum, it must be ensured that changes in the shape of the spectrum introduced by the normalization do not impede comparability. This applies in particular to the use of the total area, Euclidian norm, as well as the SNV. Any additional emission that is not accounted for by the normalization during calibration, will severely impact calibration performance for univariate techniques. Moreover, we believe that any normalization that transforms the spectrum differently depending on the concentration is inherently inadequate for univariate calibration, especially when comparing performance at different ablation atmosphere pressures, since the pressure directly impacts the line width of the F I emission.

For the normalization to the maximum, a concentration dependence can also be assumed, especially if the maximum in the spectrum coincides with the analyte line used for quantification. The minimum, on the other hand, is a sensible candidate in principle, since it is generally not correlated with the analyte, but rather to the overall plasma emissivity and background in the spectrum. However, as the minimum coincided which the outermost pixel

acquired by the spectrometer/detector and was therefore *far away* from the analyte lines, the minimum was not investigated as normalization approach either.

This leaves the normalization to the background as a prospect for this investigation. As indicated in section 3.2 of the main manuscript, we found that the wavelength range from 686.4 to 686.7 nm was comparatively feature-less and was by and large independent of the ablation atmosphere pressure apart from a change in absolute intensity. Moreover, the spectra of the investigated samples also contained no significant emission in this range. Hence, this region is particularly viable as a background.

It is important to specify what is meant by background in the context of this investigation. Due to the highly structured nature of the spectrum even in standards without added F, we summarize the baseline (continuum) and the presumed to be polymeric contributions in the collective term background. Dyar et al. [3] provide an excellent overview of baseline removal methods commonly employed in the LIBS community and in particular for geological samples, but similar to normalization, there is no general consensus on which approach is best. They compare different baseline removal algorithms, e.g., asymmetric least squares, fully automatic baseline correction, polynomial filtering and many more. Most of the approaches are implemented in the pybaselines Python package [4] and can easily be tested. However, as Dyar et al. point out in their discussion, there is no definitive criterion to compare different methods, especially as there are a large amount of parameters that can be optimized for each model. Ultimately, they conclude that the published methods perform "remarkably similar" for their data and suggest that the use of multivariate techniques instead as they are generally able to detect regions within the spectrum with predictive power, making them more stable. [3]

We indeed investigated most of the methods outlined in [3] utilizing the median values given in the reference and affirm that the results are very similar for our data. All methods were able to fit a smooth baseline to the data, which is why a lengthy discussion of the different approaches was omitted. In this work, seeing that the most attention was given to the F I emission line with the highest intensity, a simple linear baseline was fitted around this emission line by calculating the average intensity within 685.15-685.25 and 685.95-686.05 nm, respectively, and using these values as anchor points. This approach performed comparable to the more sophisticated approaches when calculating the sum intensity within 685.4-685.9 nm and was ultimately chosen as the background (not baseline) subtraction method due to its simplicity and reduced computational effort. The performance of this local linear background

approach can be examined by looking at Figure 8c) and f) of the main manuscript, where the background-subtracted spectra are compared for reduced and atmospheric pressure.

What is also clear from the spectra in Figure 8 in the main manuscript is that the F I emission line at ~685.7 nm is partially overlapping with a feature of the non-specific background, which forms a shoulder to the right of the peak. Furthermore, the height of this shoulder seems to depend on the ablation atmosphere pressure. In general and like for most plasmas, the profile of a LIBS emission line can be modelled as a Voigt profile. The effects that result in the line profile and how fundamental plasma parameters can be derived from the profiles have been discussed in detail in the literature (cf., for instance, [5,6]) and would go way beyond the scope of this work. In short, the main broadening mechanisms of a LIBS emission line are related to the Doppler and Stark effect as well as instrumental broadening, which either contribute to the Gaussian or Lorentzian portion of the Voigt profile. [7,8] Due to their preferable properties for calculation, pseudo-Voigt profiles (a linear combination of a Gaussian and Lorentzian replacing the convolution) are typically used to approximate the experimental line profile with high accuracy. For example, Aguilera et al. [9] found a relative difference of 1.5 % for the area of the pseudo-Voigt and Voigt profiles in a Cu-based alloy target in air using a Nd:YAG laser at its fundamental wavelength with a pulse energy of 100 mJ.

Here, we perform peak deconvolution as a way to reduce the contribution of the background to the evaluation of the F I emission at ~685.7 nm by fitting two pseudo-Voigt line profiles to the background-subtracted spectra. To improve the robustness of the fit, all five repeat measurements of all 8 calibration standard were fitted simultaneously by minimizing the global residual for all pseudo-Voigt profiles. Ultimately, the result was a globally determined center μ, width σ, and weighting factor η for the pseudo-Voigt profile of the F I emission (denoted as analyte) as well as the peak from the background (denoted as matrix), where the amplitudes varied for each replicate and standard. The amplitudes of the analyte profiles were then employed as a metric for univariate calibration. More information on the fitting procedure can be found in the next section (S7).

S7. Pseudo-Voigt Fitting Python Script

The Pseudo-Voigt fitting routine was implemented in the Python project outlined in section 1 and is provided below. Each spectrum of a calibration series (i.e., all spectra of the repeat measurements of the calibration standard at a specific ablation atmosphere pressure) were modeled as:

$$I(\lambda) = A_a \cdot PV(\mu_a,\sigma_a,\eta_a) + A_a \cdot PV(\mu_m,\sigma_m,\eta_m) \#(S1)$$

where PV denotes a pseudo-Voigt profile (with an equal width for the Lorentzian and Gaussian) normalized to an area of unity, A the amplitude of the pseudo-Voigt profile, the suffix a the contribution of the analyte, i.e., the F I emission, and the suffix m the contribution of the matrix, i.e., the shoulder to the right of the F I emission.

Peak centers (μ), peak widths (σ), and the mixing parameters (η) were treated as global parameters, whereas the amplitudes were allowed to vary individually. The objective function minimized the residuals of all spectra by using the Levenberg-Marquardt algorithm.

```
import numpy as np
import lmfit

def gaussian(
    x: np.ndarray,
    mu: float,
    sigma: float
) -> np.ndarray:
    g = np.exp(-0.5 * ((x - mu) / sigma)**2) / (sigma * np.sqrt(2*np.pi))
    return g

def lorentzian(
    x: np.ndarray,
    mu: float,
    gamma: float
) -> np.ndarray:
    l = gamma / np.pi / ((x - mu)**2 + gamma**2)
    return l

def pseudo_voigt(
    x: np.ndarray,
    mu: float,
    sigma: float,
    eta: float
) -> np.ndarray:
    g = gaussian(x, mu, sigma)
    l = lorentzian(x, mu, sigma)

    pv = eta * l + (1 - eta) * g
    return pv

def global_residual(
    params: lmfit.Parameters,
    x: np.ndarray,
    spectra: np.ndarray
) -> np.ndarray:
    resid = []
```

```
    # ---- global peak parameters ----
    mu_a    = params['mu_a']
    mu_m    = params['mu_m']
    sigma_a = params['sigma_a']
    sigma_m = params['sigma_m']
    eta_a   = params['eta_a']
    eta_m   = params['eta_m']

    for i, y in enumerate(spectra):
        Aa = params[f'Aa_{i}']
        Am = params[f'Am_{i}']

        model = (
            Aa * pseudo_voigt(x, mu_a, sigma_a, eta_a) +
            Am * pseudo_voigt(x, mu_m, sigma_m, eta_m)
        )

        resid.append(y - model)

    r = np.concatenate(resid)

    return r

def make_global_params(
    n_spectra: int,
    mu_a_init: float,
    mu_m_init: float,
    sigma_a_init: float = 0.2,
    sigma_m_init: float = 0.2,
    eta_init: float = 0.4
) -> lmfit.Parameters:

    params = lmfit.Parameters()

    # Add global parameters
    params.add('mu_a', value=mu_a_init,
               min=mu_a_init - 0.05, max=mu_a_init + 0.05)

    params.add('mu_m', value=mu_m_init, min=mu_m_init - 0.05, max=mu_m_init + 0.05)

    params.add('sigma_a', value=sigma_a_init,
               min=0.02, max=0.3)

    params.add('sigma_m', value=sigma_m_init,
               min=0.02, max=0.3)

    params.add('eta_a', value=eta_init,
               min=0, max=1)

    params.add('eta_m', value=eta_init,
               min=0, max=1)

    # Add variable, per-spectrum parameters (i.e., the amplitudes
    # of the analyte and matrix contribution).
    for i in range(n_spectra):
        params.add(f'Aa_{i}', value=10, min=0)
        params.add(f'Am_{i}', value=50, min=0, max=250)

    return params

# Dummy wavelength array with one dimension with a size corresponding
# to the amount of wavelengths recorded.
wavelength = np.array([])

# Dummy array containing the background-corrected spectra with
# two dimensions. The first corresponds to the amount of spectra
```

```
# used for calibration (number of repeat measurements times number
# of standards). The size of the second dimension is equal to that
# of the wavelength array.
processed_spectra = np.array([[]])

wavelength_range = (685.2, 686.0)

mask = (wavelength >= wavelength_range[0]) & (wavelength <= wavelength_range[1])

analyte_center_guess = 685.65
matrix_center_guess = 685.8

params = make_global_params(
    n_spectra=len(processed_spectra),
    mu_a_init=analyte_center_guess,
    mu_m_init=matrix_center_guess
)

result = lmfit.minimize(
    global_residual,
    params,
    args=(wavelength[mask], processed_spectra[:, mask]),
    method='leastsq'
)
```

S8. Discussion of Different Definitions for the Limit of Detection

In this section, the different approaches for determining the limit of detection (LOD) are defined, which are compared in this work. First, the following expression corresponds to the definition of the LOD by the International Union of Pure and Applied Chemistry:

Equation S1

$$y_L = \bar{y}_B + k \cdot s_B \Rightarrow y_L - \bar{y}_B = k \cdot s_B \Leftrightarrow c_L \equiv LOD = \frac{k \cdot s_B}{b}$$

y_L is the smallest discernible signal, $\bar{y}_B$ the average response due to the background, k a numerical factor that represents the desired confidence level (usually 3 or 3.3), s_B the standard deviation of blank measurements, and b the slope of the linear range of the calibration curve, which follows the model function:

Equation S2

$$y = a + b \cdot x$$

a is the intercept of the linear regression function. In their review on LIBS methodology and instrumentation, Hahn and Omenetto recommend the use of a definition that also includes information on the signal-to-background and signal-to-background noise, by using the following equation [2,10]:

Equation S3

$$c_L = k \cdot c_0 \cdot RSD_B \cdot \frac{1}{\frac{\bar{y}_S}{\bar{y}_B}}$$

c_0 is the known concentration of a measured standard, RSD_B is the relative standard deviation of blank measurements, and $\bar{y}_S$ the average response due to signal (of the analyte). Substituting RSD_B by the definition of the relative standard deviation of the signal results in the following expression:

Equation S4

$$c_L = k \cdot c_0 \cdot \frac{s_B}{\bar{y}_B} \cdot \frac{1}{\frac{\bar{y}_S}{\bar{y}_B}} = k \cdot \frac{c_0 \cdot s_B}{\bar{y}_S}$$

In its guidelines, the International Council for Harmonisation of Technical Requirements for Pharmaceuticals for Human Use (ICH) provides a further alternative by replacing the standard deviation of the blank by the residual standard deviation of a regression line or the standard deviation of the intercepts of regression lines. [11] In principle, the latter calls for repeat

calibration experiments, constructing separate regression lines, and calculating the standard deviation of the resulting intercept. For a single calibration curve, this quantity can be estimated from the standard error of its intercept, SE_a. This results in the following equation:

Equation S5

$$c_L = k \cdot \frac{SE_a}{b}$$

Finally, Hubaux and Vos published a further definition of the LOD that additionally considers the confidence limits of the linear calibration line. [12] Graphically, the definition corresponds to the concentration, at which (the value in the signal domain of) the lower confidence limit is larger than the upper confidence limit at the intercept. Considering that there is no direct analytical solution of the equation for the LOD, this graphical interpretation is typically employed to calculate the LOD by drawing a horizontal line at the upper confidence limit at zero concentration (the so-called decision limit) and determining the intersection point with the band of the lower confidence limit. [12] Interestingly, this is more akin to the limit of quantification (cf., for instance, [13]), making it the most conservative of the definitions discussed here.

S9. Univariate Models: Calibration

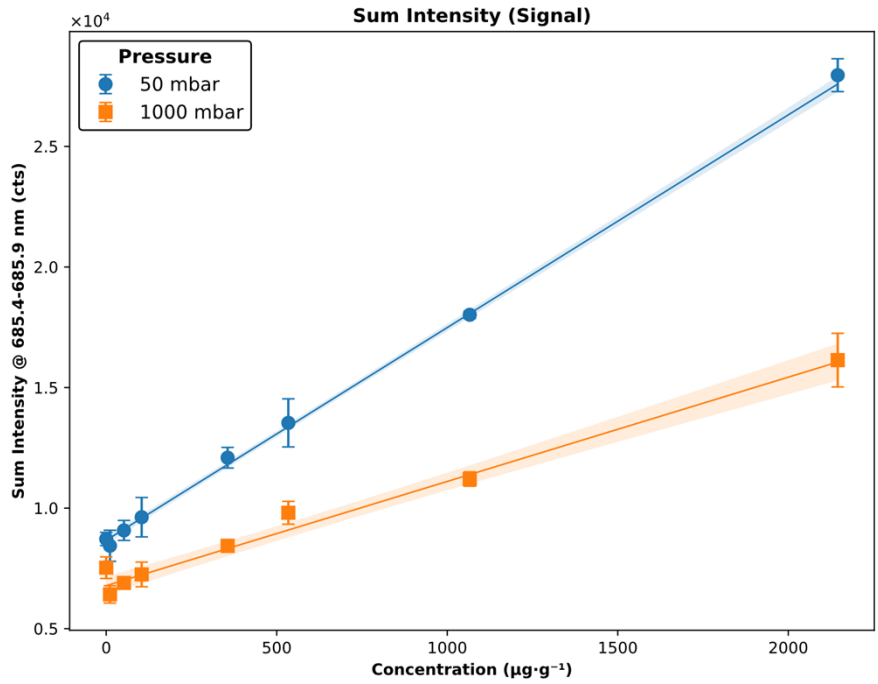

Figure S6: Comparison of calibration curves at different pressures using the sum intensity within 685.4-685.9 nm after subtraction of a local linear background.

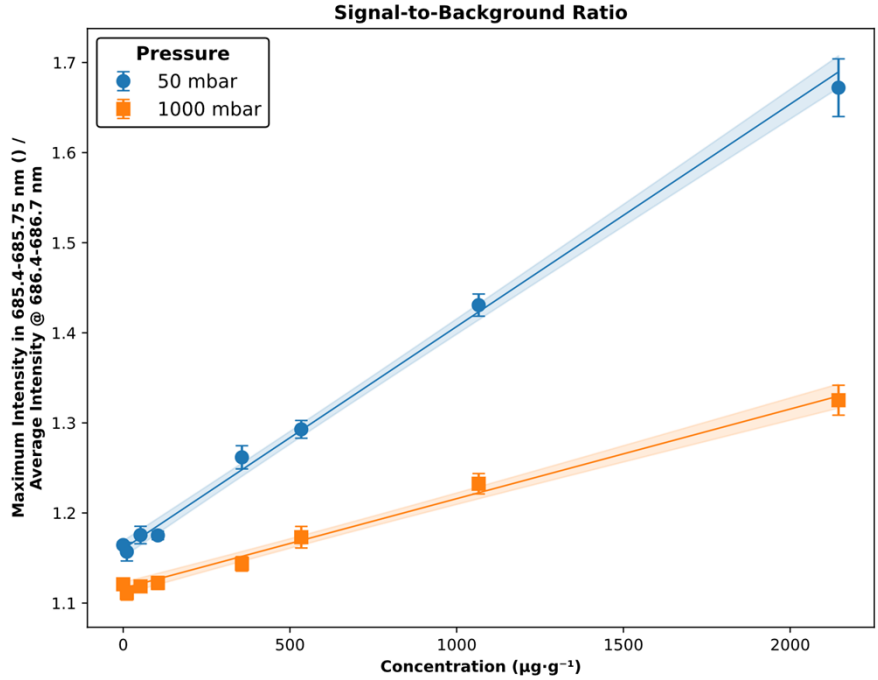

Figure S7: Comparison of calibration curves at different pressures using the signal-to-background ratio comparing the maximum intensity within 685.4-685.75 nm to the average intensity in the background region (686.4-686.7 nm).

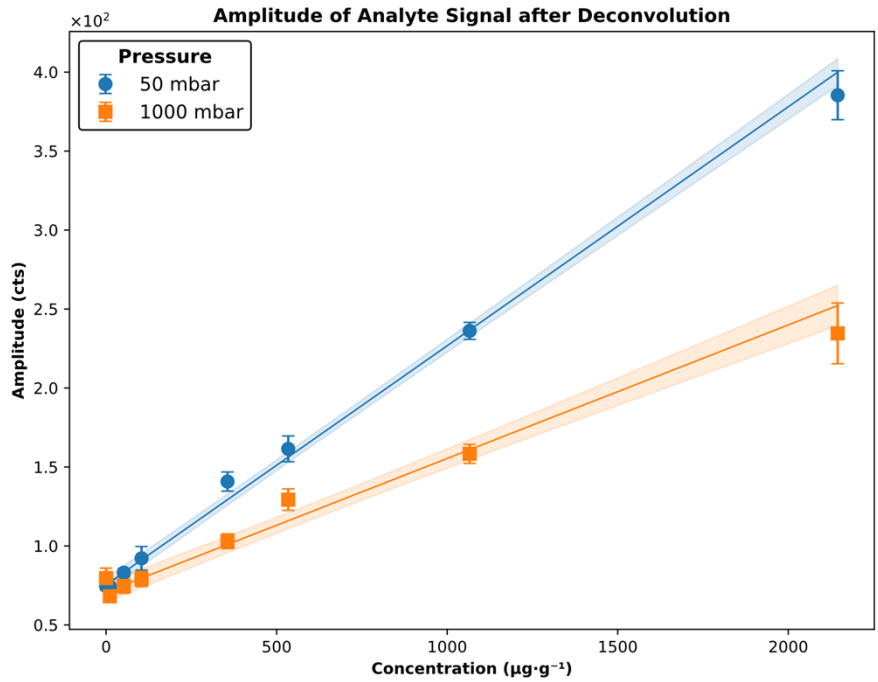

Figure S8: Comparison of calibration curves at different pressures using the amplitude of the analyte signal after background subtraction and subsequent peak deconvolution into two pseudo-Voigt line profiles.

S10. PLS: Method Development

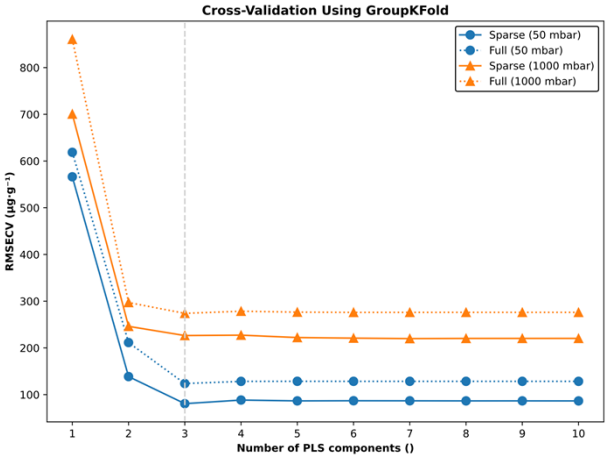

Figure S9: Cross-Validation results for the full and sparse spectrum models at different ablation atmosphere pressures.

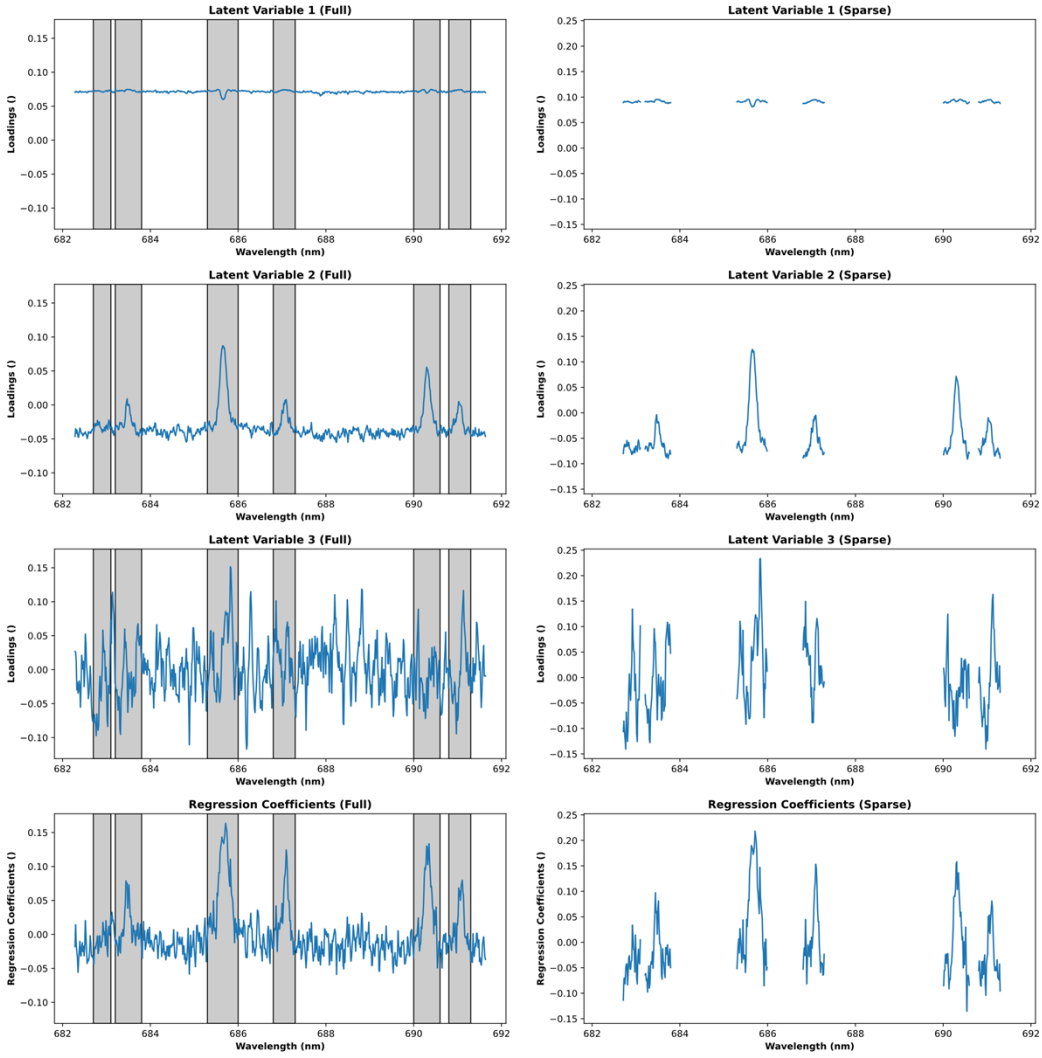

Figure S10: Comparison of full spectrum (left) and sparse spectrum (right) PLS models. Rows 1-3: loadings of the latent variables; row 4: regression coefficients.

S11. PLS: Reference versus Predicted Plots

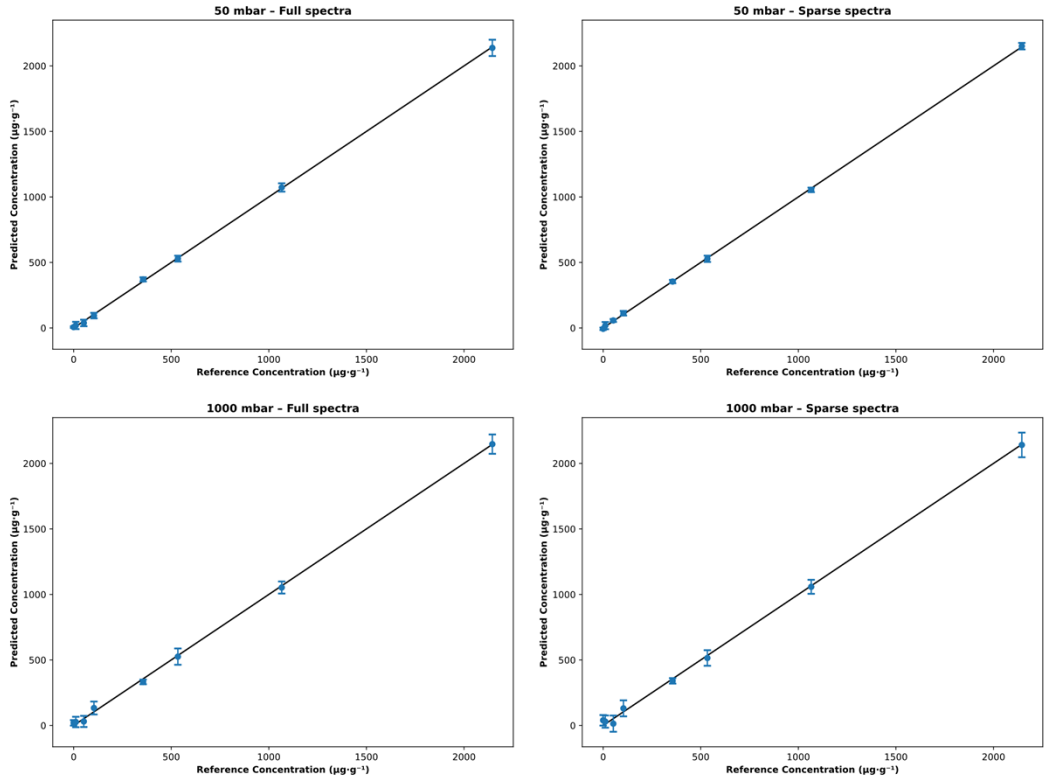

Figure S11: Reference versus Predicted plots for the full and sparse spectrum PLS models at different ablation atmosphere pressures. The error bars indicate the standard deviation of the five repeat measurement of one standard.

S12. Spectra Comparison for Polyimide Samples

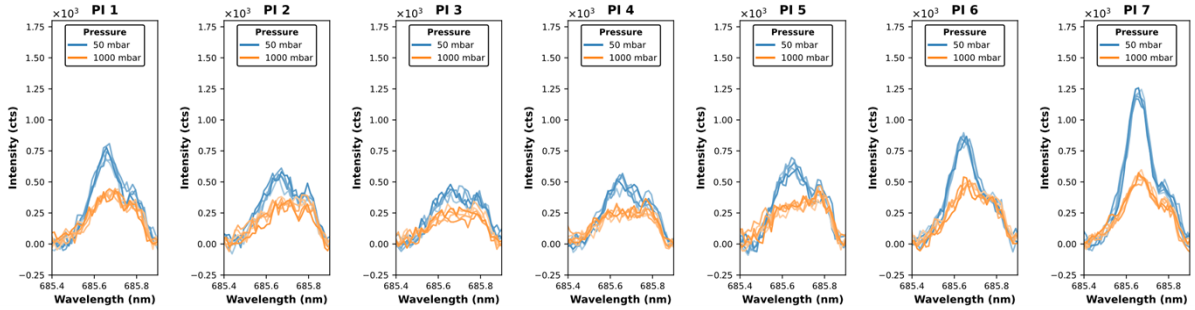

Figure S12: Spectra comparison of the polyimide samples (with background subtraction) at different pressures. Spectra represent the average of 82 shots acquired with a laser energy of 8.21 mJ, a gate delay of 0.4 µs and a gate width of 2.0 µs.

S13. Univariate Models: Concentration in Samples

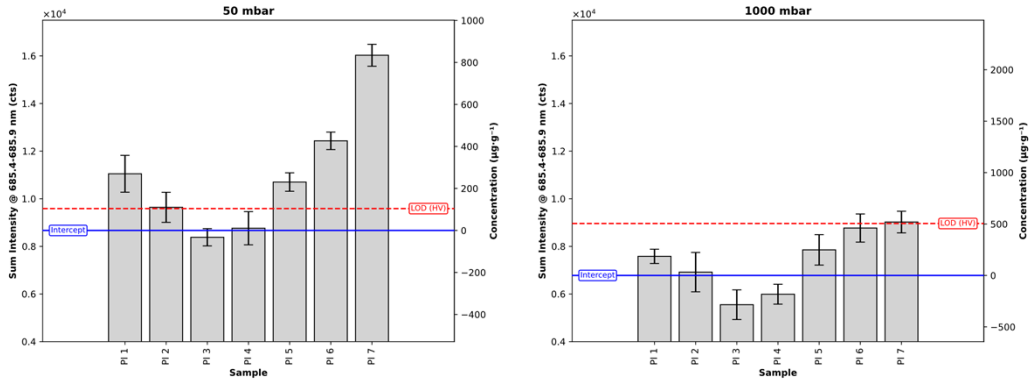

Figure S13: Sum intensity (left ordinate) and calculated concentration (right ordinate) of polyimide samples at reduced (left subplot) and atmospheric pressures (right subplot) using the sum within 685.4-685.9 nm after subtraction of a local linear background.

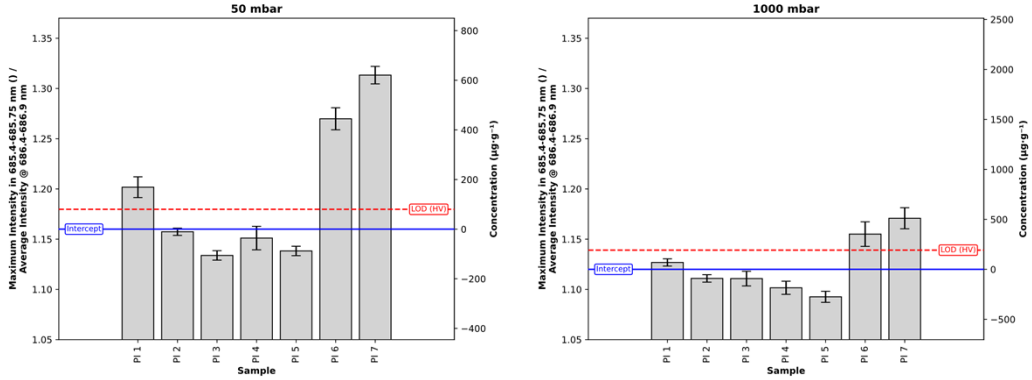

Figure S14: Signal-to-background ratio (left ordinate) and calculated concentration (right ordinate) of polyimide samples at reduced (left subplot) and atmospheric pressure (right subplot) comparing the maximum intensity within 685.4-685.75 nm to the average intensity in the background region (686.4-686.7 nm).

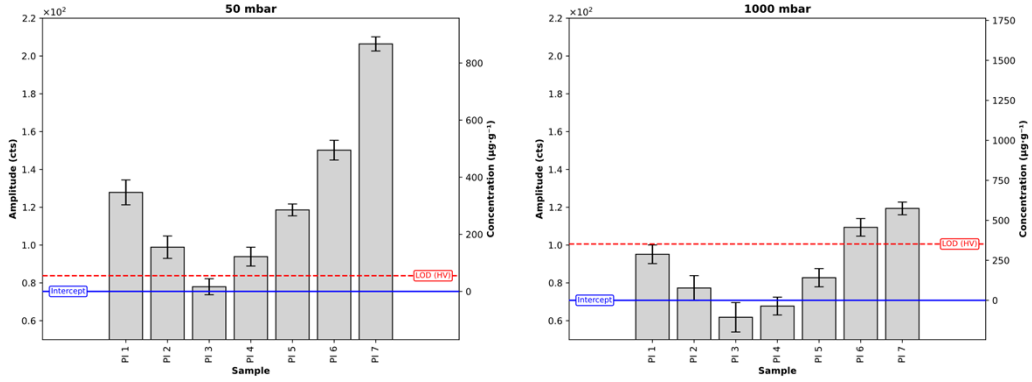

Figure S15: Amplitude of the analyte signal (left ordinate) and calculated concentration of polyimide samples (right ordinate) at reduced (left subplot) and atmospheric pressure (right subplot) after performing background subtraction and subsequent peak deconvolution into two pseudo-Voigt line profiles.

S14. PLS: Concentration in Samples

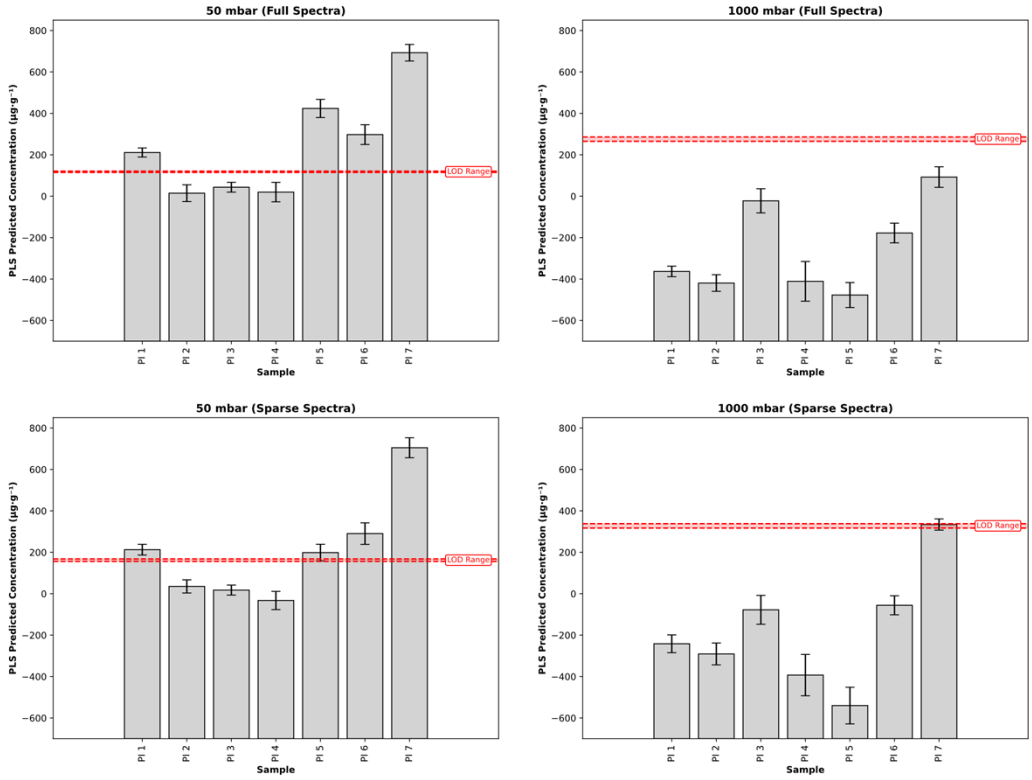

Figure S16: Determined concentration of polyimide samples at 50 mbar (left column) and 1000 mbar (right column) using the corresponding full spectrum (top row) and sparse spectrum models (bottom row).

References

[1] Guezenoc, J.; Gallet-Budynek, A.; Bousquet, B. Critical review and advices on spectral-based normalization methods for LIBS quantitative analysis. *Spectrochimica Acta Part B: Atomic Spectroscopy* **2019**, *160*, 105688. DOI: https://doi.org/10.1016/j.sab.2019.105688.

[2] Hahn, D. W.; Omenetto, N. Laser-Induced Breakdown Spectroscopy (LIBS), Part II: Review of Instrumental and Methodological Approaches to Material Analysis and Applications to Different Fields. *Applied Spectroscopy* **2012**, *66* (4), 347-419. DOI: https://doi.org/10.1366/11-06574.

[3] Dyar, M. D.; Giguere, S.; Carey, C. J.; et al. Comparison of baseline removal methods for laser-induced breakdown spectroscopy of geological samples. *Spectrochimica Acta Part B: Atomic Spectroscopy* **2016**, *126*, 53-64. DOI: https://doi.org/10.1016/j.sab.2016.10.018.

[4] *pybaselines: A Python library of algorithms for the baseline correction of experimental data (v1.2.1)*; 2025. https://doi.org/10.5281/zenodo.16790579 (accessed 03.02.2026).

[5] Griem, H. R. Spectral line broadening. In *Principles of Plasma Spectroscopy*, Griem, H. R. Ed.; Cambridge Monographs on Plasma Physics, Cambridge University Press, 1997; pp 54-131.

[6] Hahn, D. W.; Omenetto, N. Laser-Induced Breakdown Spectroscopy (LIBS), Part I: Review of Basic Diagnostics and Plasma—Particle Interactions: Still-Challenging Issues within the Analytical Plasma Community. *Applied Spectroscopy* **2010**, *64* (12), 335A-336A. DOI: https://doi.org/10.1366/000370210793561691.

[7] Ewusi-Annan, E.; Melikechi, N. Unsupervised fitting of emission lines generated from laser-induced breakdown spectroscopy. *Spectrochimica Acta Part B: Atomic Spectroscopy* **2021**, *177*, 106109. DOI: https://doi.org/10.1016/j.sab.2021.106109.

[8] Díaz Pace, D. M. Laser-induced plasma characterization using line profile analysis of chromium neutral atom and ion transitions. *Journal of Quantitative Spectroscopy and Radiative Transfer* **2013**, *129*, 254-262. DOI: https://doi.org/10.1016/j.jqsrt.2013.06.023.

[9] Aguilera, J. A.; Aragón, C.; Cristoforetti, G.; et al. Application of calibration-free laser-induced breakdown spectroscopy to radially resolved spectra from a copper-based alloy laser-induced plasma. *Spectrochimica Acta Part B: Atomic Spectroscopy* **2009**, *64* (7), 685-689. DOI: https://doi.org/10.1016/j.sab.2009.06.002.

[10] International Union of Pure and Applied Chemistry. limit of detection. In *IUPAC Compendium of Chemical Terminology*, International Union of Pure and Applied Chemistry, 2025.

[11] International Council for Harmonisation of Technical Requirements for Pharmaceuticals for Human Use. *Validation of Analytical Procedures: Text and Methodology (ICH Q2(R1) Guideline)*; International Council for Harmonisation, 2005. https://database.ich.org/sites/default/files/Q2%28R1%29%20Guideline.pdf (accessed 03.02.2026).

[12] Hubaux, A.; Vos, G. Decision and detection limits for calibration curves. *Analytical Chemistry* **1970**, *42* (8), 849-855. DOI: https://doi.org/10.1021/ac60290a013.

[13] Zorn, M. E.; Gibbons, R. D.; Sonzogni, W. C. Weighted Least-Squares Approach To Calculating Limits of Detection and Quantification by Modeling Variability as a Function of Concentration. *Analytical Chemistry* **1997**, *69* (15), 3069-3075. DOI: https://doi.org/10.1021/ac970082i.